Electronic Supplementary Information (ESI)

Rational design for broad near-infrared emission from a two-sited $Rb_2LiAlF_6:Cr^{3+}$ phosphor with high efficiency and thermal stability for spectroscopic applications

Song Qing,[a] Jing Wan,[a] Tao Yang,[a] Qiang Zhou,*[a] Yayun Zhou,[b] Zhengliang Wang,*[a] Dawei Wen,[c] Mingmei Wu*[d]

[a.] Key Laboratory of Green Chemistry Materials in University of Yunnan Province, Yunnan Key Laboratory of Chiral Functional Substance Research and Application, School of Chemistry and Environment, Yunnan Minzu University, Kunming 650500, P. R. China.

[b.] Guangdong-Hong Kong-Macao Joint Laboratory for Intelligent Micro-Nano Optoelectronic Technology, School of Physics and Optoelectronic Engineering, Foshan University, Foshan 528225, China.

[c.] School of Applied Physics and Materials, Wuyi University, Jiangmen 529020, P. R. China.

[d.] School of Chemical Engineering and Technology, Sun Yat-Sen University, Zhuhai 519082, P. R. China.

Corresponding Author:

*Email: q-zhou@ymu.edu.cn (Q. Zhou)

wangzhengliang@foxmail.com (Z. L. Wang)

ceswmm@mail.sysu.edu.cn (M. M. Wu)

The EPR signal is always employed to verify the presence and the valence state of chromium by calculating the *g*-factor from the equation of $g = \frac{h\nu}{\beta H}$, where *h*, *ν*, *β*, and *H* refer to the Planck constant, the electromagnetic wave frequency of 9.85144 GHz, the Bohr magneton, and the average difference in the magnetic field, respectively. According to the above equation, the *g* value is calculated to be 1.997 in this case (Figure S3), which ensures the presence of trivalent chromium ions with an electron spin S = 3/2. The typical EPR signal coming from Cr^{3+} ions locating at the octahedral sites.[1]

The decay curves of RLAF:0.02Cr measured at different temperatures (77 K-477 K) can be well fitted into a double-exponential equation:[11]

$$I = I_0 + A_1 e^{-t/\tau_1} + A_2 e^{-t/\tau_2} \quad \text{(S1)}$$

Here, I and I_0 are the emission intensities at time t and 0, A_1 and A_2 are constants, t is the time, τ_1 and τ_2 represent the fast and slow component of the decay times. The average lifetime τ_{av} can be calculated by the following equation:

$$\tau_{av} = \frac{A_1\tau_1^2 + A_2\tau_2^2}{A_1\tau_1 + A_2\tau_2} \quad \text{(S2)}$$

The splitting degree of d^3 energy levels affects Cr^{3+} luminescent properties, which can be illustrated by the Tanabe-Sugano diagram. According to the local CF strength of *Dq*, and the peak energies of $E(^4T_{1g})$ and $E(^4T_{2g})$, the Racah parameter of *B* can be determined by estimating the *Dq*/*B* ratio using the following formula:[2,3]

$$10Dq = E\left(^4T_{2g}\right) \quad \text{(S3)}$$

$$\Delta E = E\left(^4T_{1g}\right) - E\left(^4T_{2g}\right) \quad \text{(S4)}$$

$$\frac{D_q}{B} = \frac{15\left(\frac{\Delta E}{D_q} - 8\right)}{\left(\frac{\Delta E}{D_q}\right)^2 - 10\left(\frac{\Delta E}{D_q}\right)} \quad \text{(S5)}$$

Here, $E(^4T_{1g})$, $E(^4T_{2g})$ and ΔE represent the energies of the $^4T_{1g}$ and $^4T_{2g}$ energy levels, and the energy difference between $E(^4T_{1g})$ and $E(^4T_{2g})$. Based on the two sets of excitation band locations of the RLAF:0.02Cr sample and the above equations, the *Dq*/*B* ratios were determined to be 2.15

and 2.10, respectively (Figure S7). Both values are lower than the demarcation value of 2.3, implying that the RLAF host offers weak CFs for incorporating two kinds of Cr^{3+} activators and thereby generating two sets of wide emission bands in the NIR region.

The activation energy can be calculated using the modified Arrhenius equation:[4]

$$I_T = \frac{I_0}{1 + A \cdot exp(-\frac{\Delta E}{kT})} \tag{S6}$$

where I_T and I_0 are the integral PL intensities at given temperatures of T and 298 K, respectively. A is a constant and k stands for the Boltzmann constant. The relationship between In[(I_0/I_T)-1] and 1/kT is exhibited in Fig. 3g, in which a straight fitting line with a correlation coefficient of 0.988 and a slope of −0.228 is obtained, indicating that the fitting result is trustworthy and the activation energy is calculated to be 0.228 eV.

The Huang-Rhys parameter can be calculated by the following equation:[5]

$$FWHM = \sqrt{S \times 8\ln 2} \times \hbar\omega \times \sqrt{\coth \frac{\hbar\omega}{2k\mathrm{T}}} \tag{S7}$$

where S, $\hbar\omega$, T and k present the Huang-Rhys parameter, the mean phonon energy, the Kelvin temperature, and the Boltzmann constant, respectively. Substituting $\frac{\hbar\omega}{kT} \approx 10^{-3}$ and $\left(e^{\frac{\hbar\omega}{kT}} - 1\right) \approx \frac{\hbar\omega}{kT}$ into the above equation, it could be transformed to the following fomula:

$$FWHM^2 = 5.57 \times S \times (\hbar\omega)^2(1 + \frac{2kT}{\hbar\omega}) \tag{S8}$$

Here, the formula represents as a linear equation of $y = ax + b$, in which $y = FWHM^2$, $a = 5.57 \times S \times \hbar\omega$, $x = 2kT$, and $b = 5.57 \times S \times (\hbar\omega)^2$. Based on the temperature-dependent PL spectra, a linear fitting curve with a high correlation coefficient of 0.998 is obtained after plotting $FWHM^2$ *versus* $2kT$, as shown in Fig. 3h, indicating that the fitting results are highly reliable. According to the slope of the linear curve, S and $\hbar\omega$ are determined to be 2.64 and 14.9 meV respectively, suggesting that the RLAF host offers a weak EPC effect surrounding Cr^{3+} activators.

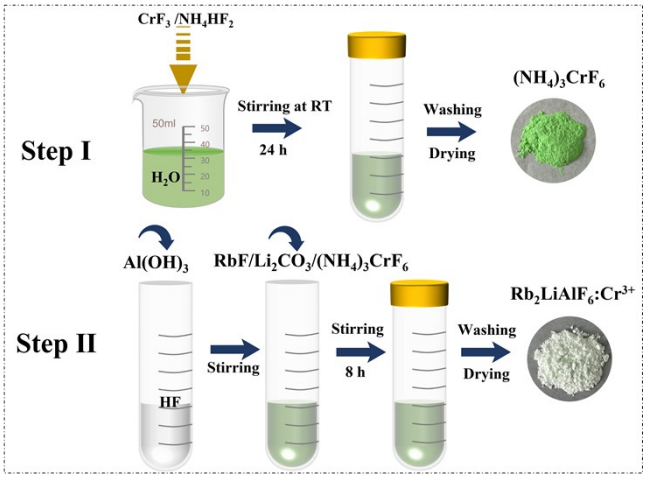

Figure S1. Schematic illustration of the preparation process.

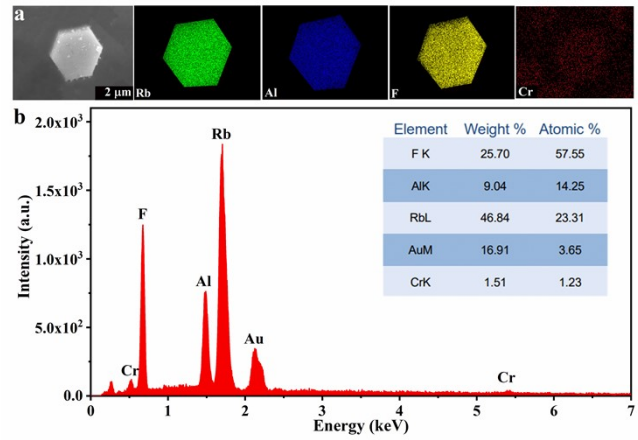

Figure S2. (a) SEM image, elemental distribution results and (b) EDS spectrum of RLAF:Cr sample.

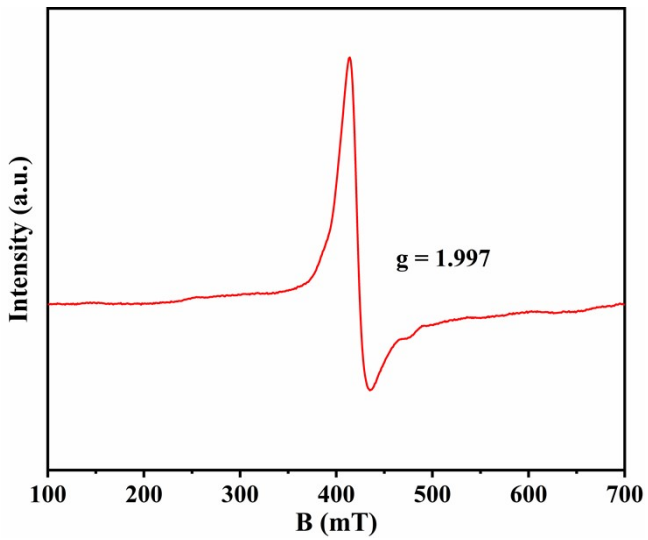

Figure S3. EPR spectrum of RLAF:0.02Cr product recorded at RT.

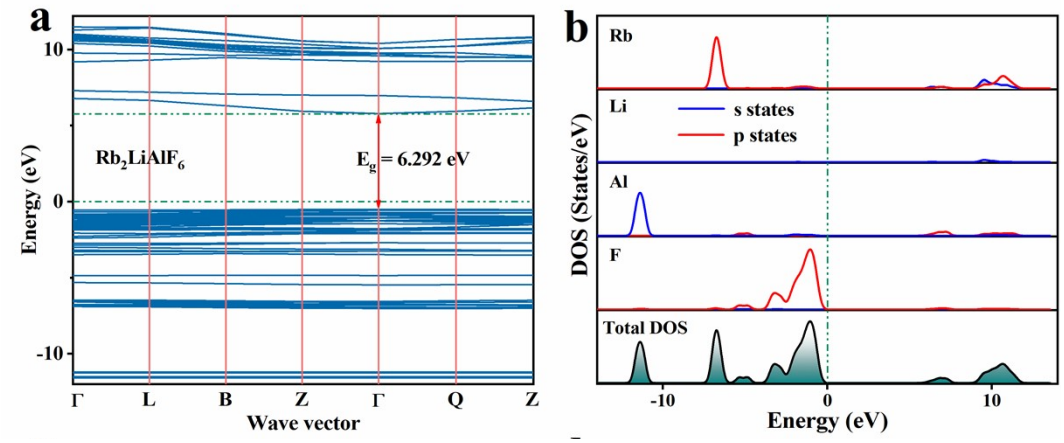

Figure S4. (a) Band structure, (b) partial and total densities of states of RLAF host.

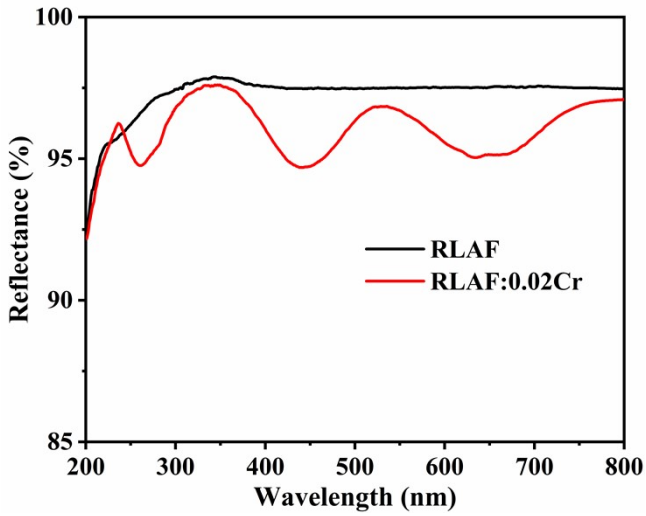

Figure S5. DRS spectra of RLAF host and RLAF:0.02Cr phosphor recorded at RT.

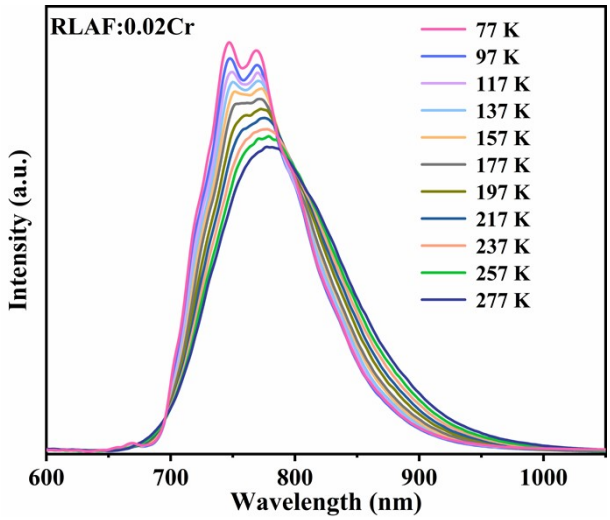

Figure S6. Temperature-dependent PL spectra of RLAF:0.02Cr recorded from 77 to 277 K.

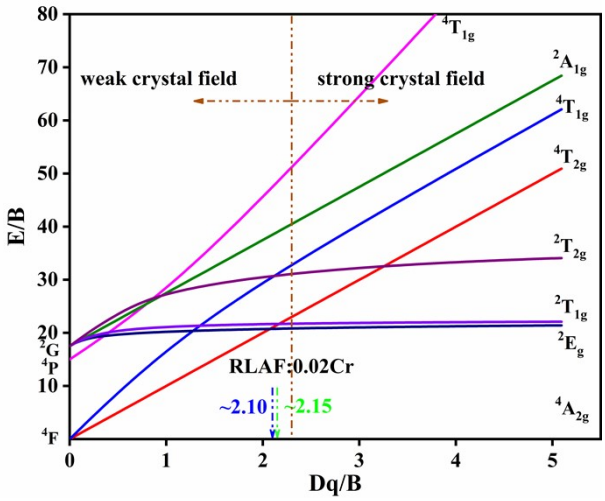

Figure S7. Tanabe-Sugano energy level diagram of Cr^{3+} in RLAF host.

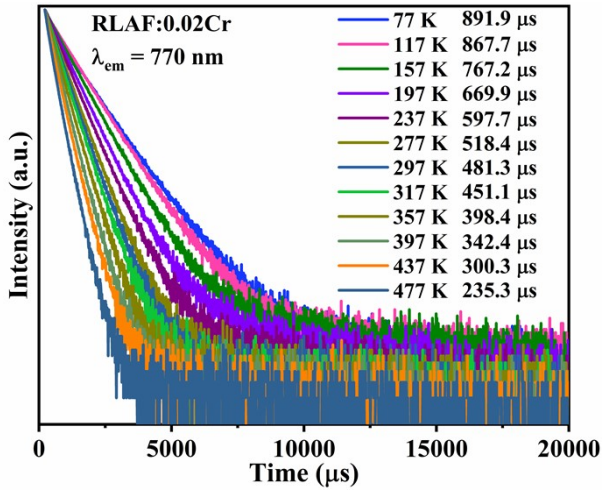

Figure S8. Decay curves of the RLAF:0.02Cr sample monitored at 770 nm from 77 K to 477 K.

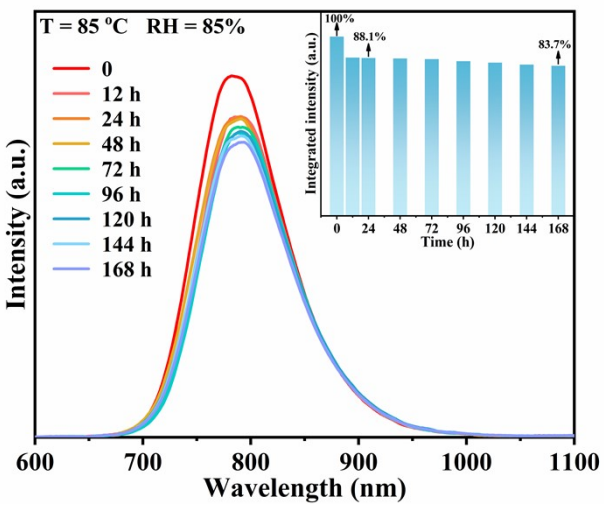

Figure S9. PL spectra and integral PL intensity variation of RLAF:0.02Cr in a high temperature (85 °C) and 85% relative humidity (RH) environment over time for 168 h.

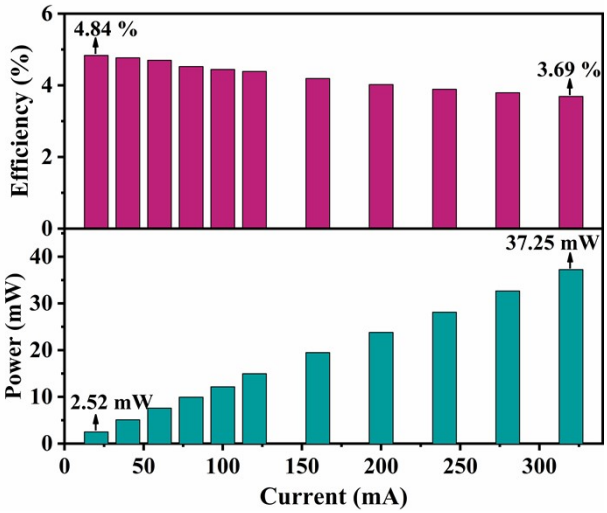

Figure S10. Photoelectric conversion efficiency and output power of the NIR pc-LED at different drive currents.

Table S1. Refined structural parameters of RLAF:0.02Cr sample.

Atom	Site	*x*	*y*	*z*	Occ.	Uiso (Å^2)
Rb(I)	6c	0	0	0.1275(4)	0.2089	0.0089
Rb(II)	6c	0	0	0.2822(4)	0.2139	0.0125
Li	6c	0	0	0.3958(4)	0.2651	0.0051
Al(I)	3a	0	0	0	0.9451	0.0033
Al(II)	3b	0	0	0.5	0.9336	0.0068
F(I)	18h	0.1412(2)	-0.1412(2)	0.4605	0.6786	0.0170
F(II)	18h	0.1813(2)	-0.1813(2)	0.6292	0.6992	0.0270
Cr(I)	3a	0	0	0	0.0549	0.0034
Cr(II)	3b	0	0	0.5	0.0664	0.0029

Table S2. Crystallographic data of RLAF:0.02Cr (Rietveld refinement result) and RLAF host.

Formula	RLAF:Cr	RLAF
Crystal system	Trigonal	Trigonal
Space group	$R\bar{3}m$	$R\bar{3}m$
$a = b$ (Å)	5.8092(3)	5.7192
c (Å)	28.0803(9)	27.8655
V (Å)	851.5471	789.41
$\alpha = \beta$	90^o	90^o
γ	120^o	120^o
Z	6	6
R_p(%)	7.20	
R_{wp}(%)	9.08	
gof	1.98	

Table S3. Luminescent properties of a selection of Cr^{3+}-doped fluoride NIR phosphors.

Phosphor	Emission peak (nm)	FWHM (nm)	$I_{150\,℃}/I_{RT}$ (%)	QE (%)	Ref.
$ScF_3:Cr^{3+}$	853	140	85.5	45	1
$K_2NaScF_6:Cr^{3+}$	765	100	89.6	74	2
$Na_3Li_3In_2F_{12}:Cr^{3+}$	778	121	58	87.2	3
$Na_3Li_3Al_2F_{12}:Cr^{3+}$	752	101	82	41.9	3
$LiCaAlF_6:Cr^{3+}$	764	124	66.6	42.3	5
$LiSrAlF_6:Cr^{3+}$	820	155	55.47	52.06	5
$LiMgGaF_6:Cr^{3+}$	819	189.9	~48	42.3	6
$Na_3ScF_6:Cr^{3+}$	774	108	30	91.5	7
$K_3AlF_6:Cr^{3+}$	750	~100	~33	25	8
$K_3ScF_6:Cr^{3+}$	752	120	87.3	71.7	9
$Na_3AlF_6:Cr^{3+}$	720	95	-	75	10
$K_2NaInF_6:Cr^{3+}$	774	116	78.3	70.9	11
$Rb_2LiAlF_6:Cr^{3+}$	781	125	90.5@417 K	77.7	This work

References

1 Q. M. Lin, Q. Wang, M. Liao, M. X. Xiong, X. Feng, X. Zhang, H. F. Dong, D. Y. Zhu, F. G. Wu and Z. F. Mu, Trivalent chromium ions doped fluorides with both broad emission bandwidth and excellent luminescence thermal stability, *ACS Appl. Mater. Interfaces*, 2021, **13**, 18274-18282.

2 E. H. Song, H. Ming, Y. Y. Zhou, F. Q. He, J. C. Wu, Z. G. Xia, Q. Y. Zhang, Cr^{3+}-doped Sc-based fluoride enabling highly efficient near infrared luminescence: a case study of $K_2NaScF_6:Cr^{3+}$, *Laser Photonics Rev.*, 2021, **15**, 2000410.

3 W. D. Nie, Y. Li, J. X. Zuo, Y. K. Kong, W. F. Zou, G. Chen, J. Q. Peng, F. Du, L. Han and X. Y. Ye, Cr^{3+}-activated $Na_3X_2Li_3F_{12}$ (X = Al, Ga, or In) garnet phosphors with broadband NIR emission and high luminescence efficiency for potential biomedical application, *J. Mater. Chem. C*, 2021, **9**, 15230-15241.

4 Z. X. Wu, X. X. Han, J. Wang, Y. Y. Zhou, K. Xing, S. Cao, J. L. Zhao, B. S. Zou and R. S. Zeng, Highly efficient and thermally stable broadband near-infrared emitting fluoride $Cs_2KGaF_6:Cr^{3+}$ for multiple LED applications, *J. Mater. Chem. C*, 2022, **10**, 10292-10301.

5 D. Wu, L. L. Liu, H. Liang, H. B. Duan, W. D. Nie, J. R. Wang, J. Q. Peng and X. Y. Ye, $LiBAlF_6:Cr^{3+}$ (B = Ca, Sr) fluoride phosphors with ultra-broad near-infrared emission for NIR pc-LEDs, *Ceram. Int.*, 2022, **48**, 387-396.

6 W. D. Nie, J. X. Zuo, S. Yang, Y. Li, W. F. Zou, G. Chen, S. H. Wu, D. Wu, S. B. Liu, J. Q. Peng, L. Han and X. Y. Ye, Ultra-broad NIR emission from two-site Cr^{3+} occupation in fluoride phosphor *via* composition-driven structural transformation, *Mater. Today Chem.*, 2022, **26**, 101164.

7 F. Q. He, E. H. Song, Y. Y. Zhou, H. Ming, Z. T. Chen, J. C. Wu, P. S. Shao, X. F. Yang, Z. G. Xia and Q. Y. Zhang, A general ammonium salt sssisted synthesis strategy for Cr^{3+}-Doped hexafluorides with highly efficient near infrared emissions, *Adv. Funct. Mater.*, 2021, **31**, 2103743.

8 C. Lee, Z. Bao, M. H. Fang, T. Lesniewski, S. Mahlik, M. Grinberg, G. Leniec, S. M. Kaczmarek, M. G. Brik, Y. T. Tsai, T. L. Tsai and R. S. Liu, Chromium(III)-doped fluoride phosphors with broadband infrared emission for light-emitting diodes, *Inorg. Chem.*, 2020, **59**, 376-385.

9 H. J. Yu, J. Chen, R. Y. Mi, J. Y. Yang, Y. G. Liu, Broadband near-infrared emission of $K_3ScF_6:Cr^{3+}$ phosphors for night vision imaging system sources, *Chem. Eng. J.*, 2021, **417**, 129271.

10 D. C. Yu, Y. S. Zhou, C. S. Ma, J. H. Melman, K. M. Baroudi, M. LaCapra and R. E. Riman, Non-rare-earth $Na_3AlF_6:Cr^{3+}$ phosphors for far-red light-emitting diodes, *ACS Appl. Electron. Mater.*, 2019, **1**, 2325-2333.

11 Z. X. Wu, X. X. Han, Y. Y. Zhou, K. Xing, S. Cao, L. Chen, R. S. Zeng, J. L. Zhao, B. S. Zou, Efficient broadband near-infrared luminescence of Cr^{3+} doped fluoride K_2NaInF_6 and its NIR-LED application toward veins imaging, *Chem. Eng. J.*, 2022, **427**, 131740.